Characterizing the temporal evolution of the high-frequency gravitational wave emission for a core collapse supernova with laser interferometric data: A neural network approach

Alejandro Casallas-Lagos,[1,2,*] Javier M. Antelis,[3,1] Claudia Moreno,[2,1,†] Michele Zanolin,[1] Anthony Mezzacappa,[4] and Marek J. Szczepańczyk[5]

[1]*Department of Physics and Astronomy, Embry-Riddle Aeronautical University, Prescott, Arizona 86301, USA*
[2]*Departamento de Física, Universidad de Guadalajara, Guadalajara, Jal., 44430, México*
[3]*Escuela de Ingeniería y Ciencias, Tecnológico de Monterrey, Monterrey, N.L., 64849, México*
[4]*Department of Physics and Astronomy, University of Tennessee, Knoxville, Tennessee 37996-1200, USA*
[5]*Department of Physics, University of Florida, PO Box 118440, Gainesville, Florida 32611-8440, USA*

(Received 25 April 2023; accepted 14 September 2023; published 11 October 2023)

We present a methodology based on the implementation of a fully connected neural network algorithm to estimate the temporal evolution of the high-frequency gravitational wave emission for a core collapse supernova (CCSN). For this study, we selected a fully connected deep neural network (DNN) regression model because it can learn both linear and nonlinear relationships between the input and output data, it is more appropriate for handling large-dimensional input data, and it offers high performance at a low computational cost. To train the Machine Learning (ML) algorithm, we construct a training dataset using synthetic waveforms, and several CCSN waveforms are used to test the algorithm. We performed a first-order estimation of the high-frequency gravitational wave emission on real interferometric LIGO data from the second half of the third observing run (O3b) with a two detector network (L1 and H1). The relative error associated with the estimate of the slope of the resonant frequency versus time for the GW from CCSN signals is within 13% for the tested candidates included in this study up to different Galactic distances (1.0, 2.3, 3.1, 4.3, 5.4, 7.3, and 10 kpc). This method is, to date, the best estimate of the temporal evolution of the high-frequency emission in real interferometric data. Our methodology of estimation can be used in future studies focused on physical properties of the progenitor. The distances where comparable performances could be achieved for Einstein Telescope and Cosmic Explorer roughly rescale with the noise floor improvements.

DOI: 10.1103/PhysRevD.108.084027

I. INTRODUCTION

We are witnessing the era of ground-based gravitational wave (GW) detectors. Since 2015, the rate of confirmed events, the sensitivity and accuracy of the GW interferometers, and the detector network, have been improved to levels that might open the door to new and complex Galactic sources of GW such as core collapse supernovae (CCSNe) (for a review, see Refs. [1,2]). A detection of GW's from CCSNe could be one of the main scientific achievements for the Advanced LIGO [3], VIRGO [4], and KAGRA [5] detectors (LVK).

CCSNe designate the final life stage for a massive star ($M_\odot > 8$), a highly energetic process of stellar explosion recorded and observed since ancient times. (For a review, see Refs. [6–11].) The explosion process begins once the star's iron core mass exceeds its Chandrasekhar limit and collapses on itself. After core collapse, a compact, dense (above nuclear matter density $1 - 2 \times 10^{14}$ g/cm^3) star is created, a protoneutron star (PNS), whose physical properties are inherited from the progenitor star. Several processes involving different regions of the PNS are associated with the generation of high-frequency (above 100 Hz) GW: convective instabilities, convective overshoot, and accretion onto the PNS (e.g., see Refs. [12–14]).

A central problem in transient GW astronomy is to reconstruct the physical parameters associated with the source of the gravitational radiation when the signal is detected in laser interferometric data. This problem involves two parts: The identification of the relevant deterministic parameters, and the best procedure to estimate them. The GW from CCSN numerical simulations manifest as strongly stochastic signals [12–51]; nevertheless, some features can be classified as deterministic. A feature that emerges from all CCSN numerical

*alejandroc.lagos@alumnos.udg.mx
†claudia.moreno@academico.udg.mx

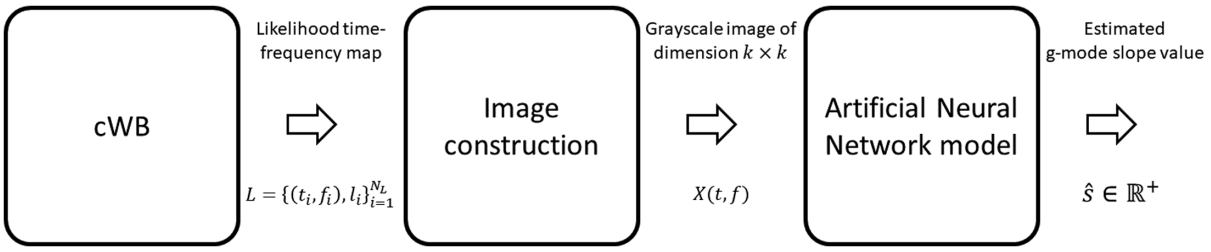

FIG. 1. Graphical description of the follow-up deep learning method proposed to estimate physical parameters of GW from CCSN events detected with cWB—specifically, the slope of the HFF oscillatory feature. The cWB pipeline detects a GW event and provides reconstructed signal information, such as the likelihood time-frequency map L. This time-frequency information is processed to construct a gray-scale image $X(t, f)$, which in turn is used as input for a deep learning regression model that estimates the value of the HFF slope, $\hat{s}$.

simulations is commonly referred to as the "*g-mode*" [13,14,16,20,24,25,27–29,31,33–35,40,44–46,49,50,52–54].

This feature is recognizable in a time-frequency spectrogram as a continuous, strictly increasing, and to a first order approximation linear feature, in the sense that, the cWB reconstructed events in current interferometric are mostly reliable for frequencies below 1000 Hz. Starting at around 100 Hz and increasing up to ∼1–2 KHz with time after bounce. Here, instead, we refer to this feature simply as the high-frequency feature, or HFF. It has been shown that the modal classification of the HFF is more complex than previously thought and can include both f and g modes [27] or possibly multiple g modes (e.g., surface and interior) [11]. The rate of increase of the HFF is a deterministic feature present in several studies focused on physical properties of the progenitor [7,27,28,50,53,55,56], parameter estimation [16,31,52,57,58], and data analysis strategies [59–63]. The first attempt to estimate the slope of the HFF with real interferometric noise was performed in [63], applying a chi-squared method to a low-order polynomial evolution of the resonant frequency. The authors applied the procedures on CCSN events identified by cWB, the flagship algorithm for the detection of GW bursts. Other studies [39,53,64], proposed an approach involving normal mode decomposition, along with a polynomial interpolation and simulated Gaussian noise, to infer the time evolution of a combination of the mass and radius of the compact remnant.

In this work we use an optimized neural network approach for the estimation of the slope of the HFF from CCSN events detected by cWB. The results of the estimation associated with the evolution of the HFF resonant frequency with time are produced in real interferometric LIGO noise, equatorial orientation, and different Galactic distances across 1.0, 2.3, 3.1, 4.3, 5.4, 7.3, and 1.0 kpc (see Tables V and VI). This aims to quantify the capability to use the slope of the HFF in different studies where numerical determination of the slope constitutes the component of a framework for parameter estimation that can be used once the GW from a CCSN are detected by the LIGO, Virgo, and KAGRA detectors.

In the rest of the text we focus our attention on the estimation of the evolution of the HFF resonant frequency with time. In order to estimate the HFF slope, we develop a deep neural network (DNN) model for regression, consisting in a set of Machine Learning (ML) algorithms that encompass diverse computational and statistical methods acting simultaneously to extract information, and to infer properties from a large variety of datasets using hierarchical structures to recognize prominent features from input data. To identify the detected events, we use Coherent WaveBurst (cWB) [65–68], a powerful computational pipeline designed to detect and reconstruct GW bursts with minimal assumptions about the morphology of the signal. We perform cWB event production on two different kinds of GW signals: The first is used to train our algorithm, providing estimated slopes associated with spectrograms in absence of noise, that reveal a linear growth of the HFF. These signals will be designated as synthetic waveforms. Once the algorithm is trained from the synthetic waveforms [52], a set of gravitational waveforms from CCSN simulations [12,13,15,16,24,27,31] are included as testing data. Figure 1 illustrates the different steps proposed in this manuscript. We quantify the accuracy of the deep learning regression model, to estimate the slope of the HFF, using the standard deviation. Graphically (see Figs. 10 and 11) a band around the mean value of the estimated slope, denoted $\hat{\bar{s}}$, in the spectrograms of the CCSN GW signals illustrates the possible outcomes of the estimation process, controlled by the standard deviation, induced by the NN model. We compute this quantity for different DNN architectures (see Table II).

The manuscript is organized as follows. Section II describes the stages for the construction of the training and testing datasets, the cWB event production analyses performed to obtain the signal detections and likelihood maps for the CCSN signals selected, the corresponding processing for the cWB outcomes, and the topology of the neural network model and the hyper-parameters that determine the performance of the neural network. In Sec. III we present the results of the implementation and the accuracy of the model. Finally, in Sec. IV we present the conclusions and future directions for this work.

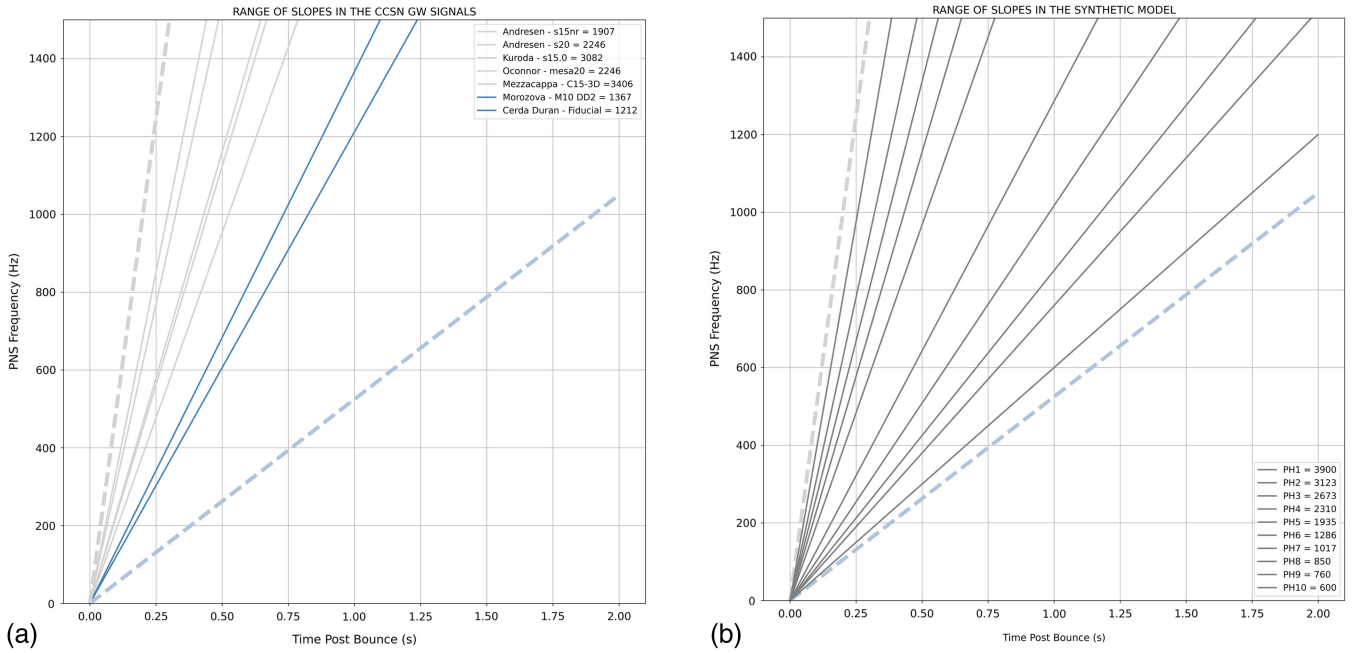

FIG. 2. Range of HFF slopes associated with (a) CCSN GW signals included in this study [see Sec. II A 2] and (b) 10 different synthetic signals [see Sec. II A 1].

II. METHODOLOGY

In this section we describe the methodology carried out to estimate the slope of the HFF fundamental resonant frequency evolution associated with CCSN GW events detected with cWB. The methodology uses (A) GW from CCSN signals, (B) the cWB algorithm to obtain likelihood time-frequency maps for detected events, (C) processing of the likelihood time-frequency maps to construct an image, and (D) the DNN model used to estimate the HFF slope value. Figure 2 illustrates the variability of the HFF slope in the synthetic, and in the GW from CCSN signals implemented in this study.

A. GW from CCSN signals

1. Synthetic signals

We created stochastic signals with increasing frequency over time, observable in their spectrograms, thus emulating CCSN GW signals containing the HFF feature. The synthetic signals are to be used in cWB event production analyses to obtain a training dataset of likelihood time-frequency maps with estimated values of the HFF slope. These signals were created based on the damped harmonic oscillator with an external stochastic driving force; i.e., a second order, nonhomogeneous differential equation, as proposed in recent work (see Eq. (1) in [52]). The solution to such differential equations is performed numerically, and the choice of several parameters such as the duration, and initial and final frequencies (which encode the HFF) can be modified easily to obtain different solution signals. Even though these synthetic signals do not carry any physical information, they are highly beneficial because it is straightforward to vary their associated parameters and because the computational cost to generate them is very low. Therefore, we can obtain signals that resemble GW from CCSN, with the HFF feature, and for each signal we directly have the value of the HFF slope, s, which is simply computed as the difference between the higher and lower frequency divided by its duration. We generated 100 different synthetic CCSN GW signals with HFF slopes ranging from 500 to 5000 Hz/s and duration ranging between $0.1s$ to $1.6s$. these values cover the range of durations found in the CCSN GW signals implemented in this study, which will be described in the next subsection. Figure 3 shows a sample of three synthetic CCSN GW signals included in this study, with HFF slope values of 626, 2319, and 4765 Hz/s.

2. Numerical simulation signals

We also used CCSN GW signals from 2D and 3D numerical simulations, all of which contain the HFF feature. This set of CCSN GW signals is used in our cWB event production analyses as a test dataset, with its estimated values of the HFF slope in the absence of noise, denoted s, computed in the following way: (i) Using the spectrogram of a CCSN GW signal, we select, for each time, the more intense pixels in its time-frequency evolution. (ii) Using the pixels described in (i), we apply a simple linear regression in the frequency range where the HFF is present. The linear regression provides the value of the slope in the absence of noise, s, along with

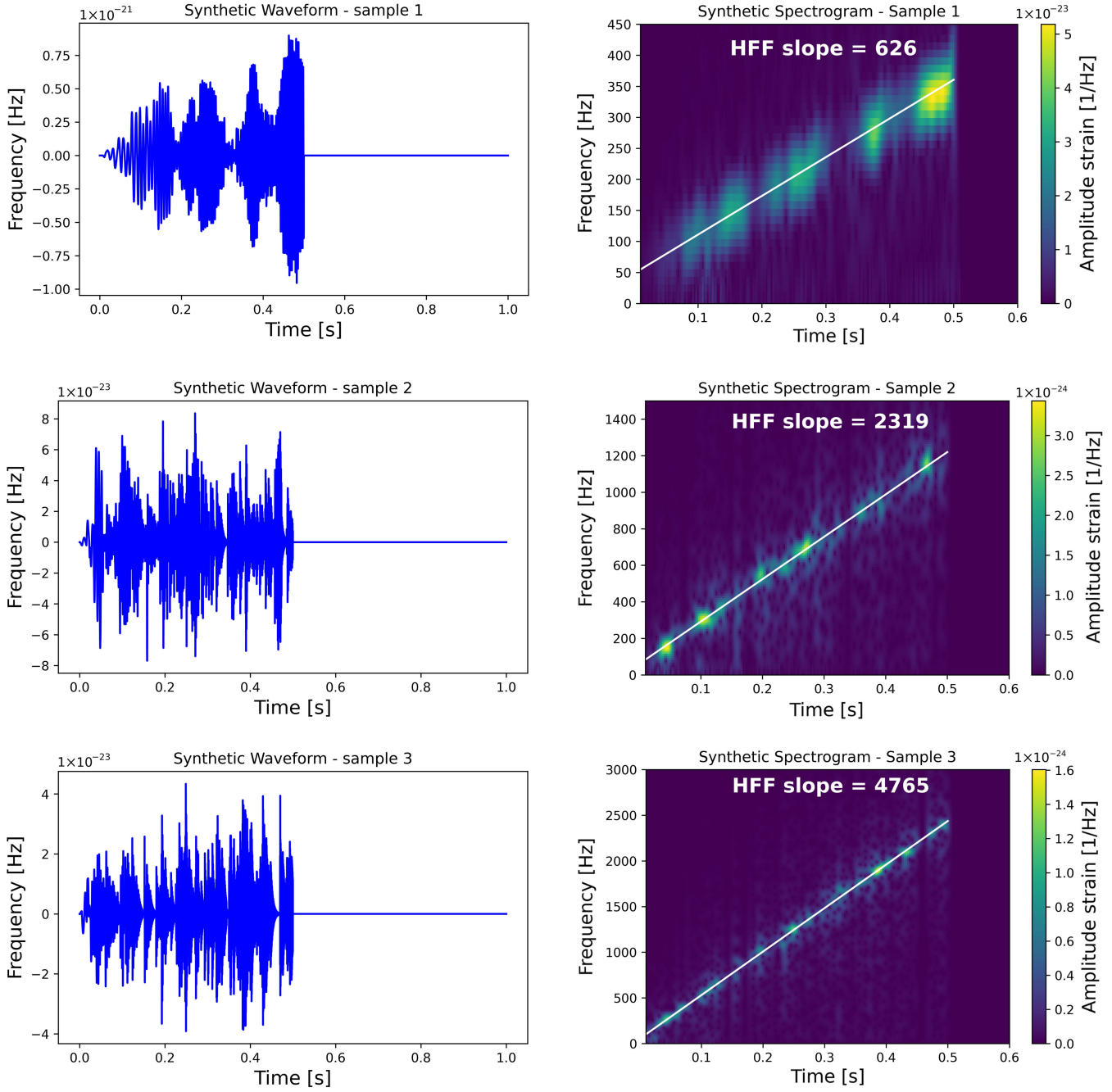

FIG. 3. Examples of three synthetic CCSN GW signals with HFF slopes of 626, 2319, and 4765 Hz/s. The amplitude and SNR of the synthetic waveforms range between 1×10^{-21} and 1×10^{-23} and between $6 < \mathrm{SNR} < 30$, respectively. Left panels show the strain signals, while the right panels shows their spectrograms. The solid white lines in the spectrograms trace the rising frequency over time.

the corresponding intercept in time. In this way, as a result of the cWB event production, every likelihood time-frequency map encodes the slope of the HFF. Specifically, we selected the following set of GW from CCSN signals computed from different progenitors and degree of rotation:

(i) Model *s20* from Andresen *et al.* [69]. The GW signal is extracted from a 3D approximately general relativistic radiation (neutrino) hydrodynamics simulation with a $20M_{\odot}$ nonrotating progenitor.

(ii) Model *s15.nr* from Andresen *et al.* [12]. The GW signals are extracted from three different models based on 3D approximately general relativistic radiation (neutrino) hydrodynamics simulations with a single progenitor with a zero-age main-sequence mass (ZAMS) of $15M_{\odot}$, solar metallicity, and with different rotation rates 0 rad/s, 0.2 rad/s, and 0.5 rad/s.

(iii) Model *Fiducial* from Cerdá-Durán *et al.* [52]. This is a GW signal generated from a 2D general relativistic

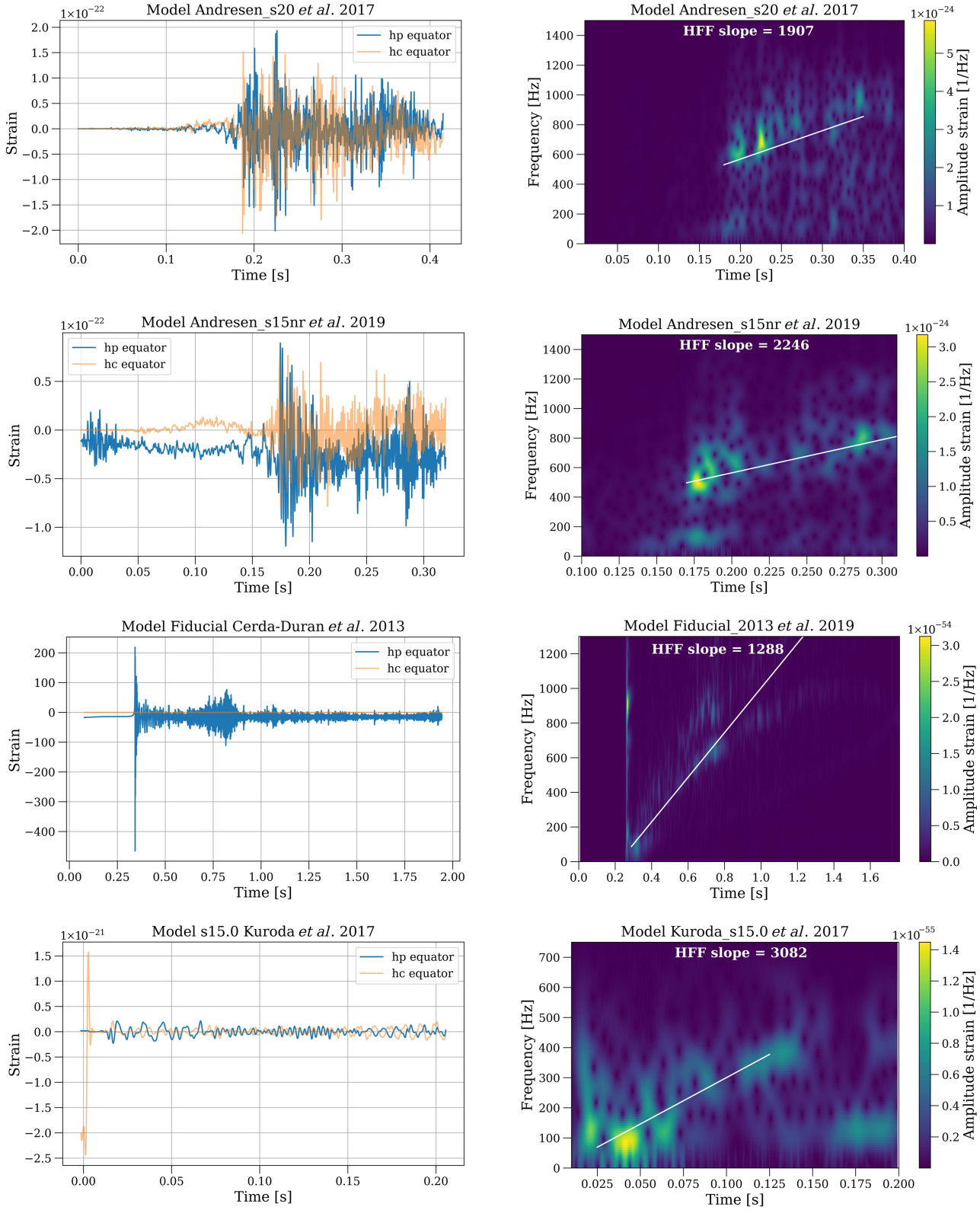

FIG. 4. Strain signals (left panels) and time-frequency evolution spectrograms (right panels) for CCSN GW models: Model *s20* from Andresen *et al.* [69], Model *s15.nr* from Andresen *et al.* [12], Model *Fiducial* from Cerdá-Durán *et al.* [52], Model *s15.0* from Kuroda *et al.* [24], Model *C15-3D* from Mezzacappa *et al.* [13], Model *M10-DD2* from Morozova *et al.* [27], and Model *mesa20* from O'Connor and Couch [31]. The solid white lines in the spectrograms trace the HFF.

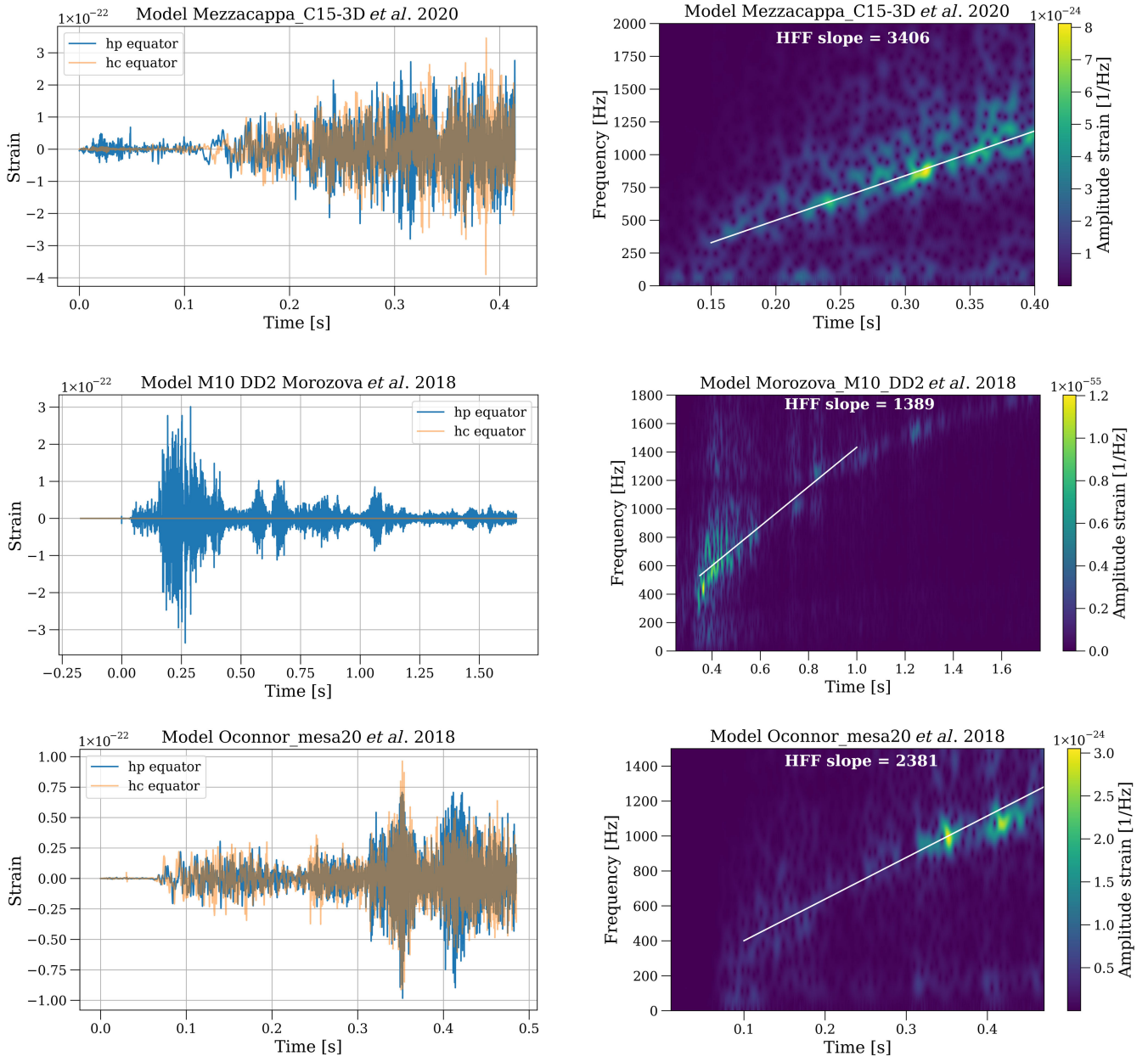

FIG. 5. Strain signals (left panels) and time-frequency evolution spectrograms (right panels) for CCSN GW models: Model *s20* from Andresen *et al.* [69], Model *s15.nr* from Andresen *et al.* [12], Model *Fiducial* from Cerdá-Durán *et al.* [52], Model *s15.0* from Kuroda *et al.* [24], Model *C15-3D* from Mezzacappa *et al.* [13], Model *M10-DD2* from Morozova *et al.* [27], and Model *mesa20* from O'Connor and Couch [31]. The solid white lines in the spectrograms trace the HFF.

hydrodynamics simulation associated with a low-metallicity, rapidly rotating progenitor, with a zero-age main-sequence mass of $35M_\odot$ whose initial central angular velocity is 2 rad/s.

(iv) Model *s15.0* from Kuroda *et al.* [24]. For this signal, the GW emission is obtained from a 3D general relativistic radiation (neutrino) hydrodynamics with a $14M_\odot$, solar metallicity, nonrotating progenitor.

(v) Model *C15-3D* from Mezzacappa *et al.* [13]. For this signal the GW emission is computed for a 3D approximately general relativistic radiation (neutrino) hydrodynamics simulation with a nonrotating $15M_\odot$ progenitor of solar metallicity.

(vi) Model *M10-DD2* from Morozova *et al.* [27]. This signal was generated from a 2D approximately general relativistic radiation (neutrino) hydrodynamics CCSN simulation with a $10M_\odot$ progenitor with solar metallicity and moderate rotation: 0.2 rad/s.

(vii) Model *mesa20* from O'Connor and Couch [31]. In this model, the GW emission is modeled from a 3D approximately general relativistic radiation

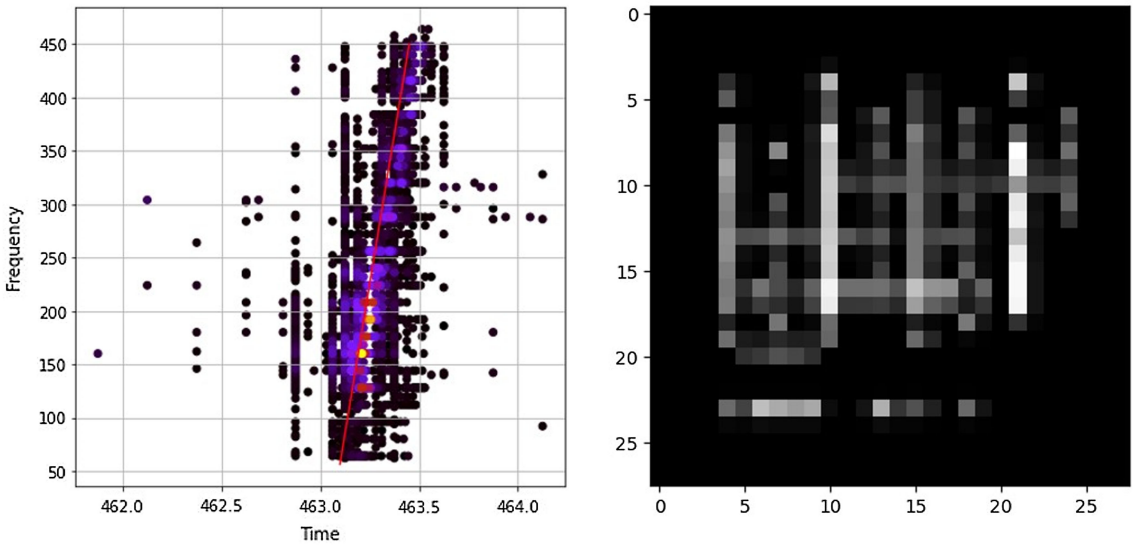

FIG. 6. Likelihood time-frequency map, L, of a detected event from a synthetic signal and its corresponding two-dimensional data matrix $X(t,f)$ of dimension $k \times k$ with $k = 28$.

(neutrino) hydrodynamics CCSN simulation with a $20M_{\odot}$, solar metallicity, nonrotating progenitor.

Note that all of these CCSN GW signals are from 3D numerical simulations except for the signals models *Fiducial* and *M10-DD2*, which correspond to 2D simulations. In addition, these signals were used in recent studies involving targeted searches [62], false detection rates [70], and sensitivity analyses of GW's from CCSNe [61], using strain data of the LIGO, VIRGO, and KAGRA detectors. Figures 4 and 5 shows the strain signals and the spectrograms of signal models *s20*, *s15.nr*, *Fiducial*, *s15.0*, *C15-3D*, *M10-DD2*, and *mesa20*. Note how the spectrograms manifest the HFF feature.

B. cWB event production

Coherent waveburst (cWB) is a standard method for detecting and reconstructing GW embedded in strain data recorded with the LIGO, VIRGO, and KAGRA detectors. The method uses minimal assumptions about the signal morphology [65–68], which has been a successful methodology in the search of "unmodeled" GW's, including those from CCSNe, although GW's from CCSNe are by now far from unmodeled. The cWB algorithm (1) searches for coincident signal power across detectors by projecting the multidetector data onto the wavelet (i.e., time-frequency) domain using the Wilson-Daubechiers-Meyer transform [71], (2) identifies a collection of coherent time-frequency components with amplitudes above noise levels, and (3) clusters them to obtain a likelihood time-frequency map $L = \{(t_i, f_i), l_i\}_{i=1}^{N_L}$, where l_i is the likelihood point value at time t_i and frequency f_i, and N_L is the number of time-frequency points. Figure 6 shows the likelihood time-frequency map L for a detected event from a synthetic GW signal. We use in this study the likelihood time-frequency map L to estimate the HFF slope value because it contains the significant time-frequency information that is used to reconstruct the detected GW signal. cWB event production analyses were performed using LIGO data from the second half of the third observing run (O3b) with a two-detector network (L1 and H1). The aim was to obtain distributions of likelihood time-frequency maps of detected GW from CCSNe, to train and to test the deep learning algorithm that estimates the value of the HFF slope. The cWB event production was developed at standard configuration [68]. Known GW from CCSN signals were injected every 50 s, at seven different Galactic distances 1.0, 2.3, 3.1, 4.3, 5.4, 7.3, and 10 kpc, with equatorial orientation, into the detector strain data on the second half of the third observing run O3b. Along this paper we use the cWB detections, and we performed the HFF slope estimation without going into the details of how the significance is assigned. The amount of detections vary depending on the injected signals, we obtained 12.221 detections for the synthetic waveforms, and 5134 detections for the GW from CCSN signals. Some relevant parameters involved in the configuration file, that controls the operation of cWB for the event production are: The optimal probability for black pixel selection, (bpp), that was set at $bpp = 0.05$, and the subnetwork threshold, ($subnet$), $subnet = 0.5$. Along with this parameters the production thresholds, *netRHO* and *netCC*, was fixed at $netrho = 4.0$ and $netCC = 0.4$. The lowest and highest frequencies were adjusted at $fLow = 100$ and $fHigh = 750$, respectively. Then, the search for GW is carried out, and for each detected event, the likelihood time-frequency map L is computed, along with some reconstructed signal attributes. All cWB event production analyses were

performed in two separate stretches of strain data. The first, comprising 1 day of coincident data, was used to obtain the training data, while the second stretch of data, comprising 8 days of coincident data, was used to obtain the testing data. In addition, our cWB analyses were performed separately with the synthetic and with the CCSN GW signals containing the characteristic HFF feature, as was described below. The set of synthetic signals constructed as part of this study (see Sec. II A 1) was used in the first stretch of strain data, to obtain the training dataset, $\mathcal{D}_{\text{train}} = \{L_j, s_j\}_{j=1}^{N_{\text{train}}}$, where L_j and s_j are the likelihood time-frequency map and the HFF slope value of the jth detected event, respectively, and N_{train} is the number of training instances. Furthermore, the set of GW from CCSN signals (see Sec. II A 2) was used in the second stretch of strain data, to obtain the test dataset of likelihood time-frequency maps, $\mathcal{D}_{\text{test}} = \{L_j, s_j\}_{j=1}^{N_{\text{test}}}$, where N_{test} is the number of test instances. It is important to remark at this point that training and test datasets are mutually exclusive, which is a necessary condition to assess the robustness of the machine learning algorithm used to perform the estimation of the HFF slope with unknown GW from CCSN signals.

C. Image construction

The likelihood time-frequency map, $L = \{(t_i, f_i), l_i\}_{i=1}^{N_L}$, varies across detected events in the number of points, the frequency range, and the time range. Therefore, it is necessary to produce a data representation with standard dimensions so that it can be used as input to the machine learning model that estimate the slope of the HFF. Hence, the goal is to define a function $f(\cdot)$ that maps L into a two-dimensional data matrix $X(t, f)$; that is, $f: L \to X(t, f)$, where the width (t-dimension) and height (f-dimension) are the same for any detected GW. Given $L = \{(t_i, f_i), l_i\}_{i=1}^{N_L}$, the image construction is carried out through the following procedure. First, we select the time-frequency point that has the maximum likelihood value, $\{t_m, f_m\}$. Then, we select a region around t_m in the interval $[t_m - \delta_t, t_m + \delta_t]$ (width in the t-dimension of $2 \cdot \delta_t$), and around f_m in the interval [50 Hz, 750 Hz], where the cWB reconstructed signal is more accurate. The length of δ_t is fixed at 0.3 s such that the time interval is large enough to contain the primary evolution of the early high-frequency HFF present in the GW from the CCSN models considered in this study [see Sec. II A 2]. This region is then transformed into a high-resolution, gray-scale image where the intensity is given by the likelihood value of the corresponding time-frequency points, while pixels with no corresponding time-frequency points are set to zero. Finally, this gray-scale image is downsized to dimension $N_r \times N_c$ to obtain the final two-dimensional data matrix or image $X(t, f)$, where N_r and N_c represent the number of rows and columns, respectively. Equivalently, the data matrix or image $X(t, f)$ can be flattened to construct the N-dimensional column vector $\mathbf{x} \in \mathbb{R}^N$, where $N = N_r \cdot N_c$. Figure 6 shows the two-dimensional data matrix $X(t, f)$, with dimension $N_r = N_c = 28$, for a likelihood time-frequency map, L, of a detected event given a synthetic signal.

D. Deep neural network model for regression

To estimate the HFF slope of CCSN GW events detected with cWB, we use a deep learning regression model. The input to this model is the column vector representation $\mathbf{x} \in \mathbb{R}^N$ of the processed likelihood time-frequency map, $X(t, f)$, while the output is the estimated HFF slope value $\hat{s}$. The HFF slope values estimated in this work are continuous, real, and positive (i.e., $s \in \mathbb{R}^+$), ranging from 500 Hz/s to 5000 Hz/s. Hence, there are several regression methods that can be used to address this task; for instance, linear and polynomial models, decision trees, and artificial neural networks [58–61,72–75]. For this study, we selected a fully connected deep neural network (DNN) regression model because it can learn both linear and nonlinear relationships between the input and output data, it is more appropriate for handling large-dimensional input data, and it offers high performance at a low computational cost. DNN are machine learning models inspired by biological neural network models of the brain, consisting of many interconnected processing units known as neurons, which vaguely mimic biological neurons [59,73,76]. The structure of a DNN comprises an input layer, one or more hidden layers, and an output layer, thus resembling a brain neural network [58–60]. The input layer consists of nodes that receive the input data and pass them directly into the first hidden layer for further processing, whereas hidden and output layers consist of many neurons [59,76] interconnected by weighted synaptic links. In a DNN, the information flows from the input toward the output while being processed in the layers, through the following function:

$$f\colon \mathbb{R}^m \longmapsto \mathbb{R}^n, \tag{1}$$

where m and n denote the number of nodes or neurons of two successive layers. Therefore, the jth neuron in a layer (hidden or output) with n neurons is connected to all of the m outputs of the preceding layer, via the weighted synaptic connections [76], in such a way that the neuron produces the output y_j as a function of linear combinations of the input information as follows:

$$y_j = g\left(\sum_{i=1}^{m} w_{i,j} x_i\right), \tag{2}$$

where $w_{i,j}$ are the weights connecting all m inputs to the jth neuron and $g(\cdot)$ is a bounded, differentiable, real, and nonlinear function known as an activation function [73,75]. The activation function allows the nonlinearity between the input–output relationship. In regression problems, typical

TABLE I. Architectural description of the deep neural network (DNN) regression models used to assess the estimation of the HFF slope from likelihood time-frequency maps.

	No. of hidden layers	No. of neurons	No. of weights
M1	1	16	12,577
M2	2	32-16	25,665
M3	3	64-32-16	52,865
M4	4	128-64-32-16	111,361
M5	5	256-128-64-32-16	244,737

activation functions are linear, sigmoid, or the rectified linear unit [76]. Note that the number of nodes of the input layer corresponds to the input variables (in our case, N inputs), the number of neurons in the output layer corresponds to the output variables (in our case, one output), whereas the number of hidden layers, the number of neurons in each layer, and the activation functions are hyper-parameters that can be freely varied to obtain different DNN models. Therefore, the synaptic weights are the parameters that are fitted from a training dataset. We considered five DNN models with different numbers of hidden layers and neurons. Table I presents the technical details of the DNN models, which are named M1, M2, M3, M4, and M5. In all models, the activation functions correspond to the rectified linear unit (ReLu) in the hidden layers and to the linear function in the output layer. The training of the models (i.e., the fitting of the synaptic weights) was based on the back-propagation learning algorithm using the root-mean-squared propagator (MNSprop) with the mean-squared error as a loss function, a learning rate of 0.001, a batch size of 512 samples of the training data, and 300 epochs.

III. RESULTS

In this section we present the results of two analyses devoted to assessing the performance of the estimation of the HFF slope of CCSN GW events using DNN regression models.

A. Hold-out cross-validation with $\mathcal{D}_{\text{train}}$

We first assessed the effectiveness and reliability of the proposed DNN model for the estimation of the HFF slope, testing the training dataset of likelihood time-frequency maps, $\mathcal{D}_{\text{train}}$, through a hold-out cross-validation (HOCV) procedure [76,77], where the entire dataset was randomly split into two parts for training (70%) and for testing (30%). This procedure was repeated 30 times to account for the randomness of the process and to be able to compute

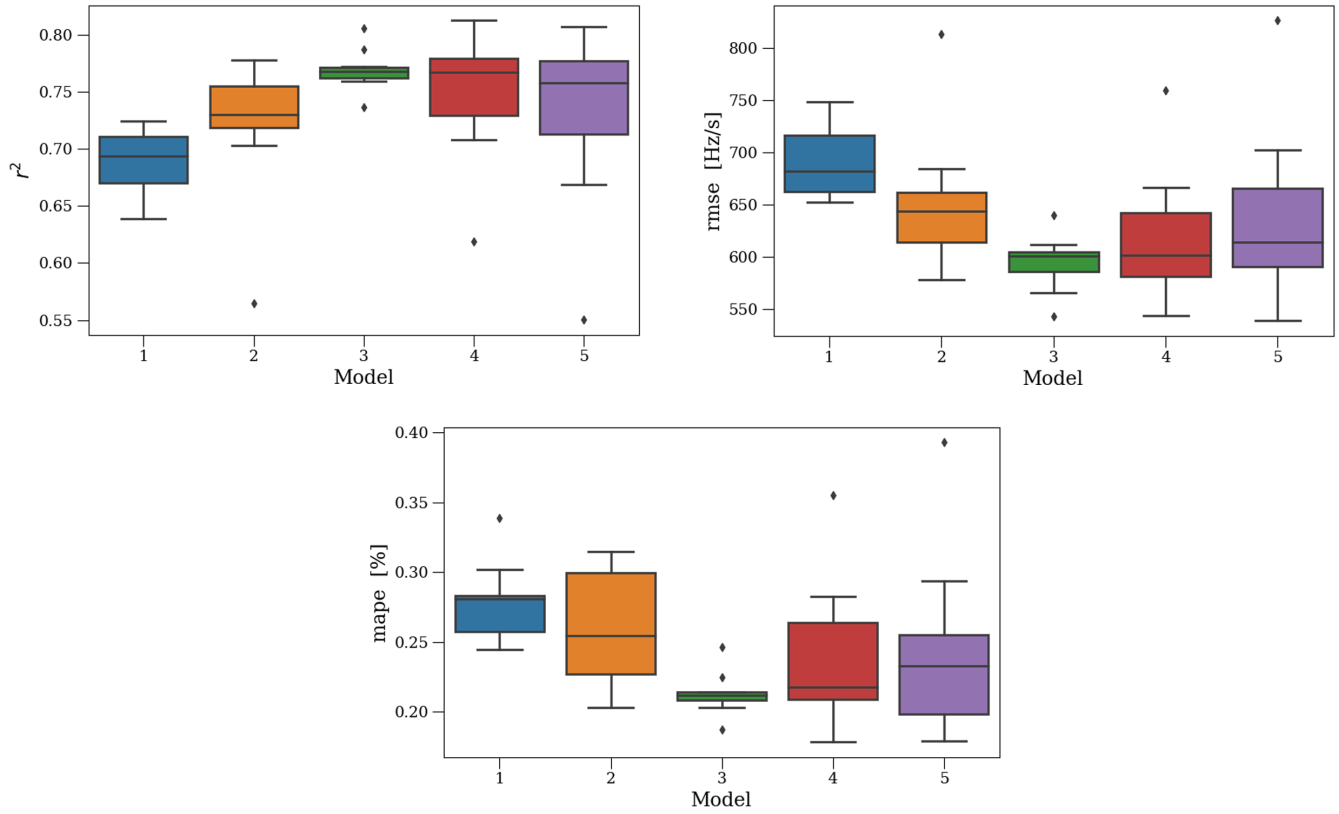

FIG. 7. Distribution of the performance metrics, r^2, RMSE, and MAPE, achieved with the five DNN regression models in the hold-out cross-validation procedure with the dataset $\mathcal{D}_{\text{train}}$. The horizontal central lines in the box plots denote the median of the estimated HFF slopes.

distributions of the performance metrics. Note that in each repetition the training and testing data are mutually exclusive. The training set is used to fit the weights of the DNN model, while the test set is used to asses the model performance [59,60]. To assess the performance, we used the following metrics: (i) the coefficient of determination (r^2), defined as:

$$r^2 = 1 - \frac{\sum_i (s - \hat{s}_i)^2}{\sum_i (s - \overline{s_i})^2}, \tag{3}$$

where $(s - \hat{s}_i)^2$ denote the sum of the squares of the residuals, $\overline{s_i} = \frac{1}{n}\sum_i s_i$ is the mean of the estimated slopes in absence of noise (for n-observations), and $(\sum_i s - \overline{s_i})^2$ corresponds to the total sum of squares. This metric measures for every model the linear correlation between the estimated slopes in absence of noise (s) present in the likelihood maps and the corresponding estimated slopes ($\hat{s}$); (ii) the root-mean-square error (RMSE) defined as:

$$\mathrm{RMSE} = \sqrt{\frac{\sum_i (\hat{s}_i - s_i)^2}{n}}. \tag{4}$$

This metric is computed, like the coefficient of determination, using the residuals, $(s - \hat{s})$. Its computation serves to discriminate how far from the mean the estimated slopes are, and finally (iii) the mean-absolute-percentage error, (MAPE), defined as:

$$\mathrm{MAPE} = \frac{100\%}{n}\sum_{i=1}^{n}\frac{|s - \hat{s}|}{s} \tag{5}$$

is a performance metric that measures the accuracy of our estimations evaluating the residuals, $(s - \hat{s})$, divided by (s) and summed over every estimated value on a certain number, (n), of observations. These performance metrics provide support to evaluate the accuracy of each model from different perspectives and clarify the outputs obtained. Table II shows the average values of the performance metrics achieved with the five DNN models.

According to the scores presented in the table, we conclude that model three (M3) (see Table I) exhibits the best performance in estimating the slope of the HFF, among the five different DNN architectures (M1 to M5), because (1) it has the higher linear correlation (0.76) expressed through the r^2 coefficient and (2) the lowest residuals (594.64) and percentage error (21%) reported by the RMSE and MAPE, respectively. Figure 7 illustrates the performance metrics for each model. Model 3 (in green) shows a lower dispersion with respect to the mean of the estimated slopes for the HFF, and lower residuals compared

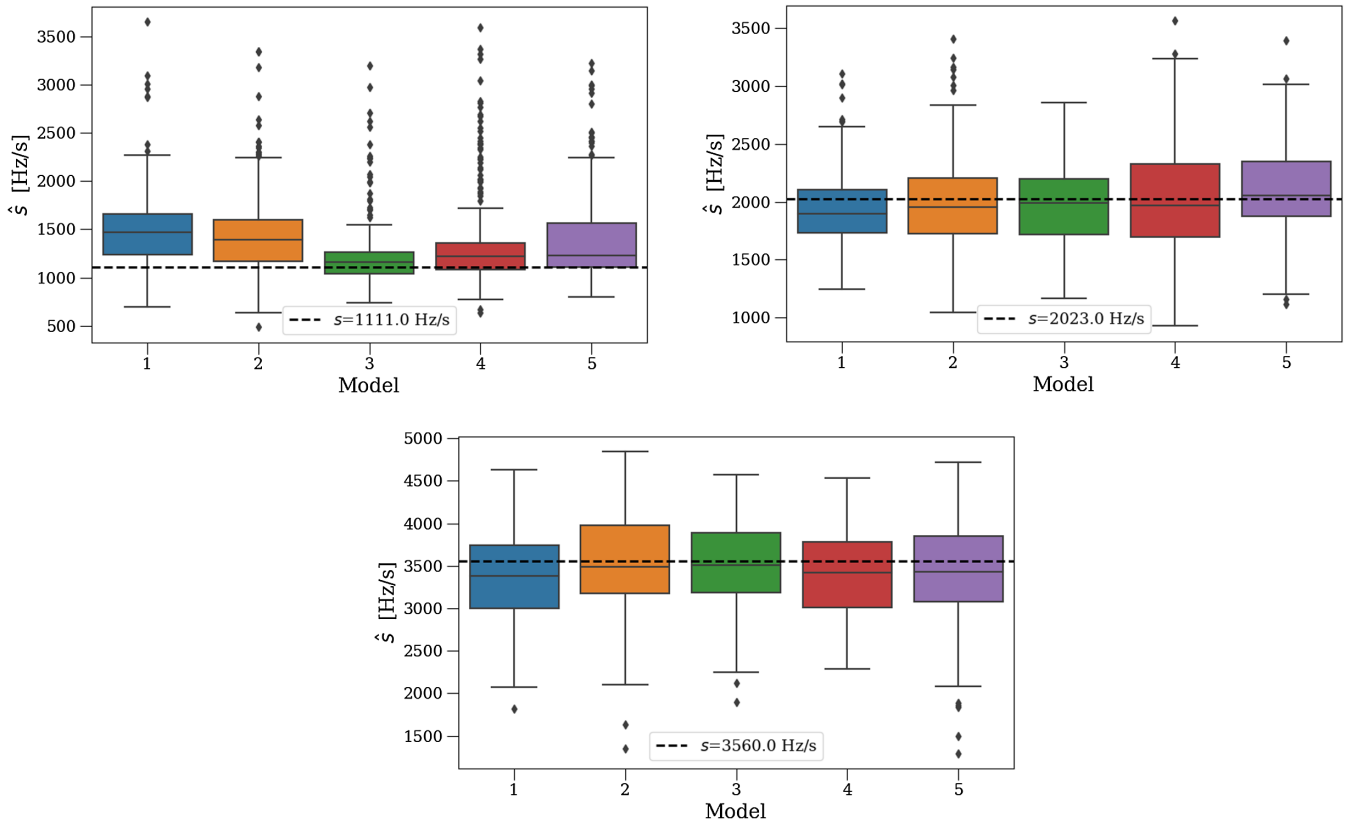

FIG. 8. Distribution of estimated values $\hat{s}$ achieved with the five DNN models in the hold-out cross-validation procedure with the dataset $\mathcal{D}_{\mathrm{train}}$ for the specific cases of real values of $s = 1111.0$ Hz/s, $s = 2023.0$ Hz/s, and $s = 3560.0$ Hz/s.

TABLE II. Summary (mean ± standard deviation) of the performance metrics, r^2, RMSE, and MAPE, achieved with the DNN regression models in the hold-out cross-validation procedure with the dataset $\mathcal{D}_{\text{train}}$.

Metric	M1	M2	M3	M4	M5
r^2	0.68 ± 0.02	0.72 ± 0.05	$\mathbf{0.76 \pm 0.01}$	0.74 ± 0.05	0.73 ± 0.07
RMSE (Hz/s)	690.57 ± 32.86	651.27 ± 65.08	$\mathbf{594.64 \pm 26.31}$	616.79 ± 62.03	636.85 ± 81.94
MAPE	0.27 ± 0.02	0.25 ± 0.04	$\mathbf{0.21 \pm 0.01}$	0.23 ± 0.05	0.24 ± 0.06

TABLE III. HFF slope estimation results. Each column contains the values associated with the slope, s, estimated slope, $\hat{s}$, plus its corresponding standard deviation, STD, its RMSE, and its MAPE. All of this is for the M3-DNN architecture.

Model	s (Hz/s)	$\hat{s}$(Hz/s) ± STD	RMSE (Hz/s)	MAPE
Fiducial from Cerdá-Durán *et al.* [52]	1288	$\mathbf{1204.78 \pm 120.75}$	142.37	0.09
s15.0 from Kuroda *et al.* [24]	3082	$\mathbf{3169.36 \pm 67.52}$	108.68	0.03
M10-DD2 from Morozova *et al.* [27]	1389	$\mathbf{1193.24 \pm 122.76}$	228.54	0.14
mesa20 from O'Connor and Couch [31]	2381	$\mathbf{2525.21 \pm 146.58}$	204.95	0.06
s15.nr from Andresen *et al.* [12]	2246	$\mathbf{2263.17 \pm 380.58}$	380.59	0.13
s20 from Andresen *et al.* [12]	1907	$\mathbf{2399.42 \pm 759.80}$	904.59	0.33
C15-3D from Mezzacappa *et al.* [13]	3406	$\mathbf{3358.91 \pm 619.03}$	719.98	0.20

with those associated with the remaining models: M1 (blue), M2 (orange), M4 (red), and M5 (purple). To give a more individual characterization of the different DNN models, Fig. 8 illustrates how distinct architectures estimate a single slope contained in the training dataset. This figure clarifies the fact that estimation performed by model M3 produces the best fit compared with the other DNN architectures.

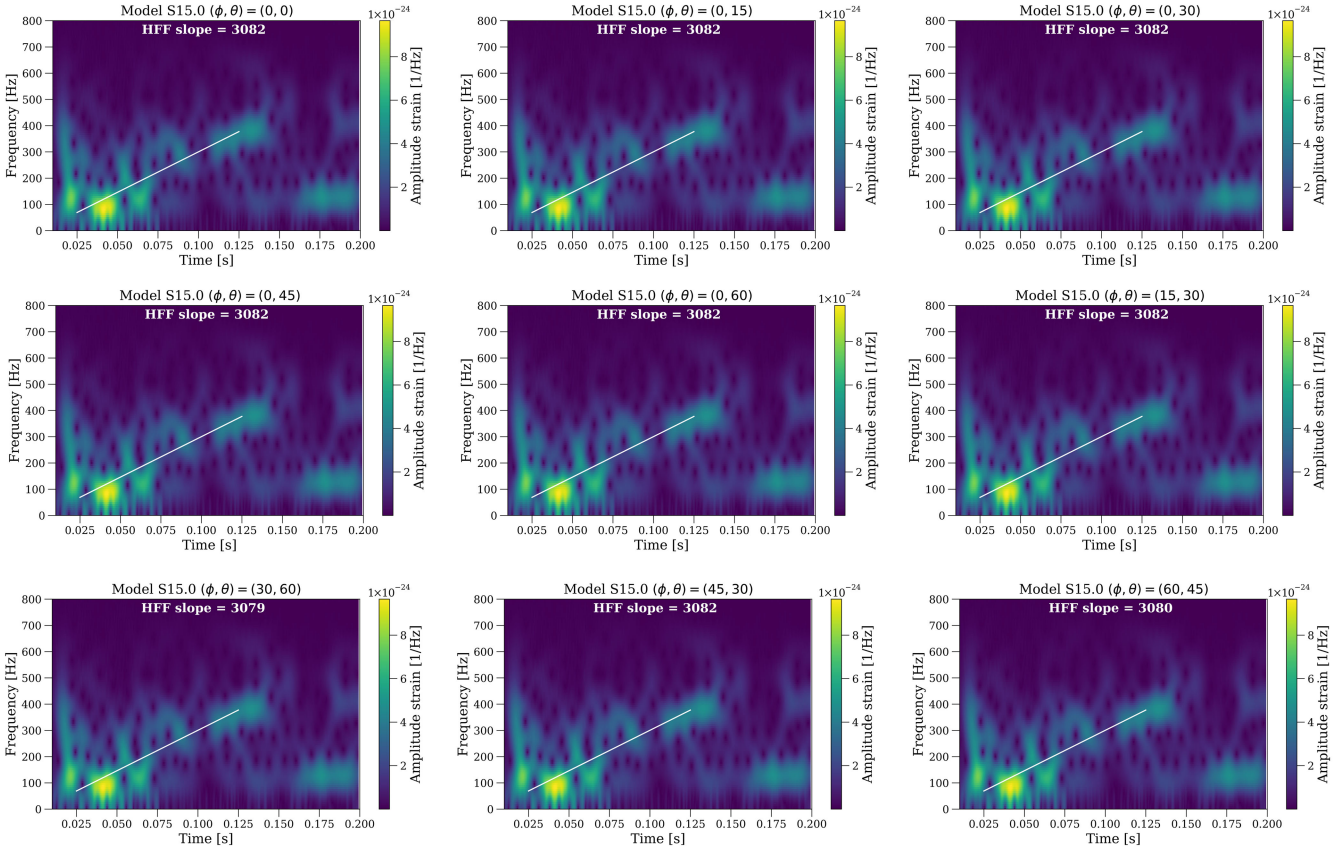

FIG. 9. Estimation of the HFF slope for model *s15.0* from Kuroda *et al.* [24], across nine different random orientations.

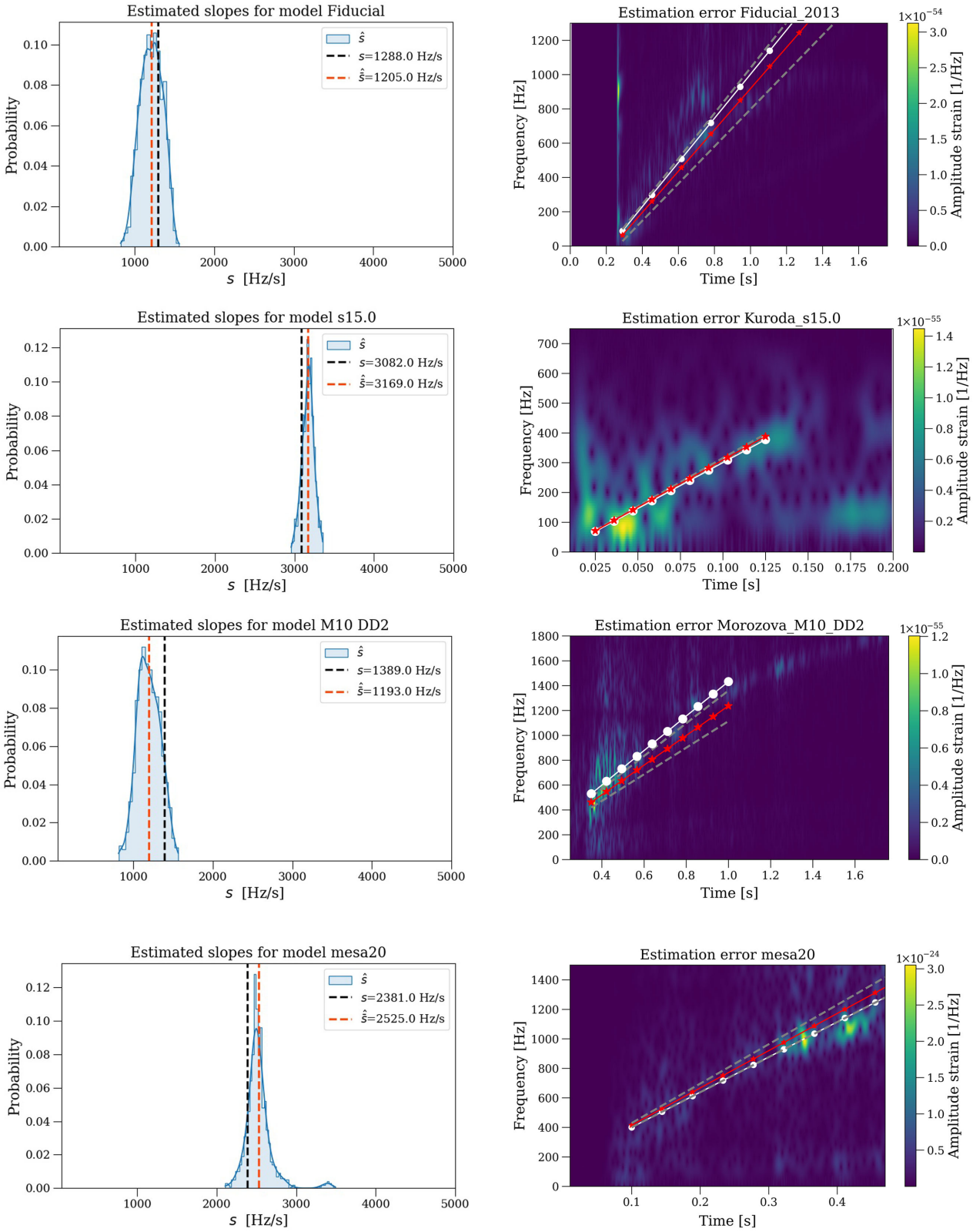

FIG. 10. HFF estimated slope, $\hat{s}$, HFF estimated slope mean, $\hat{\bar{s}}$, and their corresponding HFF estimation errors, associated with different CCSN GW signals included in this study. The histograms on the left show, in blue, the HFF estimated slopes and, with red, dashed lines, the HFF estimated means. The right column illustrates the estimation error in the spectrograms of the CCSN GW signals described in Sec. II A 2. The gray, dashed lines denote the estimation errors. White, solid lines with circles denote the slope of the HFF, in the absence of noise. And red lines with stars correspond to the mean of the estimated HFF slopes obtained through the M3-DNN architecture.

B. Estimation of the HFF slope of 3D CCSN GW signals

After the design [Sec. II], construction [Sec. II C], and successive sanity checks performed on the training dataset, $\mathcal{D}_{\text{train}}$ [Sec. III A], we use the M3-DNN architecture [see Table I], along with the processed likelihood maps for the GW from CCSN signals, as a test dataset, $\mathcal{D}_{\text{test}}$, in order to perform the estimation of the HFF slope. $\mathcal{D}_{\text{test}}$ is only composed of processed likelihood maps obtained from CCSN signals [see Sec. II A 2] that were not considered in the training process; therefore, the estimation of the HFF slope is carried out on $\mathcal{D}_{\text{test}}$, an unknown set of signals for the DNN architecture. Table II contains the performance metrics results for every model described in Sec. II D on the training dataset $\mathcal{D}_{\text{train}}$; moreover, Table III shows the results of the implementation for the DNN architecture [see Table I] on the different GW from CCSN signals included

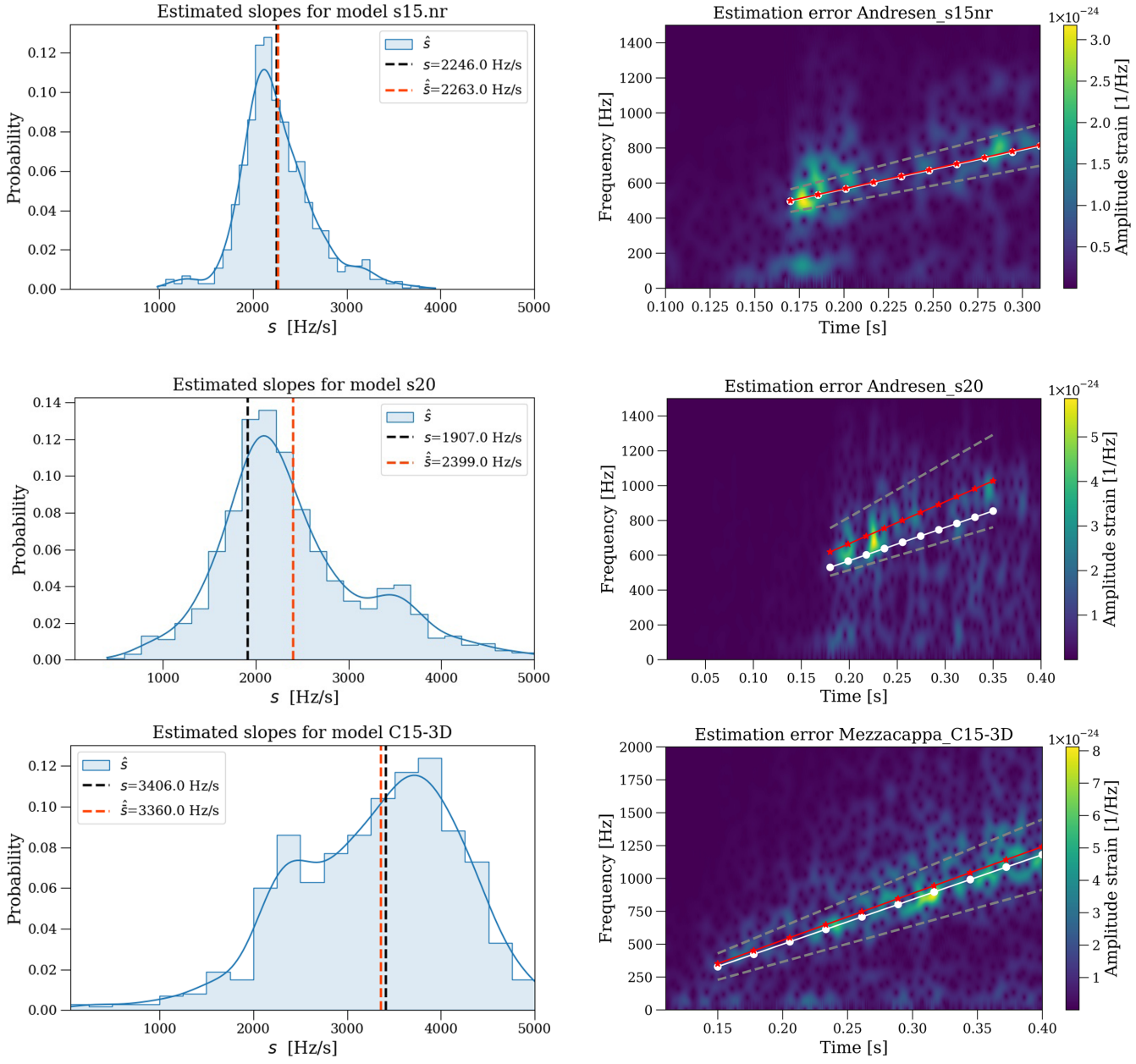

FIG. 11. HFF estimated slope, $\hat{s}$, HFF estimated slope mean, $\hat{\bar{s}}$, and their corresponding HFF estimation errors, associated with different CCSN GW signals included in this study. The histograms in the left column show, in blue, the HFF estimated slopes and, with red, dashed lines, the HFF estimated mean. The right column illustrates the estimation error in the spectrograms of the CCSN GW signals described in Sec. II A 2. The gray, dashed lines denote the estimation error. The white, solid lines with circles denote the slope of the HFF, in absence of noise. And the red lines with stars correspond to the mean of the estimated HFF slopes obtained through the M3-DNN architecture.

in this study [see Sec. II]. These results reflect a mean-absolute-percentage error, (MAPE), in the estimation of the HFF slope for this sample of 13%, which includes GW from CCSN signals for different progenitor (ZAMS) masses, metallicities, and rotation rates. To frame our results (see Table IV) we consider the variation of the HHF slope with equation of state, (EOS), progenitor mass, rotation, and metallicity. In Figs. 10 and 11, we show (left column) the histograms that describe the distribution of estimated slopes (in blue) for each CCSN GW signal included in $\mathcal{D}_{\text{test}}$. The vertical, black, dashed lines stand for the values of the HFF slope in the absence of noise, while the red, dashed lines define the estimated HFF slope means, denoted $\hat{\bar{s}}$. In the right column, the spectrogram of each CCSN GW signal illustrates the estimation error. The solid white lines with circles indicate the values of the slopes in the absence of noise, for each model. Solid red lines with stars indicate the means of the estimated slopes, $\hat{\bar{s}}$, obtained from the M3-DNN architecture. The dashed, gray lines denote the estimation errors according to the STDs reported in Table III. An estimation of the GW temporal evolution of the HFF fundamental resonant frequency for a core collapse supernova was recently presented in [63], using a chi squared approach in the context of a multimessenger analysis for the identification and parameter estimation of the standing accretion shock instability (SASI) with neutrino and GW signals. Following our methodology based on the implementation of a neural network (see Secs. II and III B), the estimation of the slope of the HFF fundamental resonant frequency for a CCSN is improved by 85% for model *s15.0* from Kuroda *et al.* [24] when compared with the value reported in the study of the SASI. This fact reveals that the implementation of a neural network model yields a substantial improvement when compared with chi-squared-based estimation. Assuming we are not aware of theoretical reasons why the HFF should have a strong dependence on the source orientation, we estimated the robustness of our results with respect to randomizing the orientation of the source. In Fig. 9 we present an example of HFF slope estimation for model *s15.0* from Kuroda *et al.* [24], considering nine different random orientations. A systematic study was performed for the remaining CSSN GW signals implemented in this paper, and the impact on the slope value varies between a few percent and 10%. For a real CCSN detection, we will have a specific orientation. The source orientation variability discussed in this paragraph will, however, have to be accounted for in future efforts to extract physical information about the progenitor.

IV. SUMMARY

We incorporate a set of synthetic CCSN GW signals (see Sec. II) to train a DNN model (Sec. III A) to estimate the slope associated with the gravitational wave temporal evolution of the HFF present in CCSN GW signals (Sec. II A 2). We quantified the accuracy of distinct DNN architectures using three different performance metrics to evaluate the accuracy of every model under different topologies, as presented in Table II, searching for the more accurate configuration to achieve estimation of the HFF slope. Our analysis and implementation of such DNN architectures indicate we can estimate the slope of the HFF in real interferometric data for different Galactic sources and CCSN GW idiosyncrasies (Sec. II A 2). Tables V and VI show the HFF slope estimation with its

TABLE IV. Variation of the HFF slope across progenitor mass, rotation, and metallicity, and across EOS.

Model	s (Hz/s)	$\hat{s}$ (Hz/s)	EOS	Mass $M_\odot$	Rotation	Metallicity
Fiducial, Cerdá-Durán *et al.* [52]	1288	**1204.78**	LS220	35	2 rad/s	Low
mesa20, O'Connor and Couch [31]	2381	**2525.21**	SFHo	20	—	Solar
s20, Andresen *et al.* [69]	1907	**2399.42**	LS220	20	—	Solar
s15.0, Kuroda *et al.* [24]	3082	**3169.36**	SFHx	15	—	Solar
C15-3D, Mezzacappa *et al.* [13]	3406	**3358.91**	LS220	15	—	Solar
s15.nr, Andresen *et al.* [12]	2246	**2263.17**	LS220	15	0.5 rad/s	Solar
M10-DD2, Morozova *et al.* [27]	1389	**1193.24**	LS220	10	0.2 rad/s	Solar

TABLE V. Variation of the HFF estimated slope across different Galactic distances: 1.0, 2.3, 3.1, and 4.3 kpc.

Model	s (Hz/s)	1.0 kpc	2.3 kpc	3.1 kpc	4.3 kpc
Fiducial, Cerdá-Durán *et al.* [52]	1288	1204.78	1345 ± 221	1575 ± 496	1954 ± 596
mesa20, O'Connor and Couch [31]	2381	2525.21	2689 ± 145	2903 ± 312	3312 ± 396
s20, Andresen *et al.* [69]	1907	2399.10	2614 ± 223	3012 ± 496	3324 ± 342
s15.0, Kuroda *et al.* [24]	3082	3169.36	3243 ± 109	3472 ± 221	3723 ± 443
C15-3D, Mezzacappa *et al.* [13]	3406	3358.91	3443 ± 237	3743 ± 396	3978 ± 234
s15.nr, Andresen *et al.* [12]	2246	2263.17	2509 ± 207	2689 ± 441	2945 ± 504
M10-DD2, Morozova *et al.* [27]	1389	1193.24	1349 ± 115	1576 ± 396	1608 ± 503

TABLE VI. Variation of the HFF estimated slope across different Galactic distances: 5.4, 7.3, and 10 kpc.

Model	5.4 kpc	7.3 kpc	10 kpc
Fiducial, Cerdá-Durán *et al.* [52]	2172 ± 598	2560 ± 698	3012 ± 723
mesa20, O'Connor and Couch [31]	3576 ± 696	3976 ± 621	4217 ± 876
s20, Andresen *et al.* [69]	3508 ± 554	4295 ± 662	4796 ± 883
s15.0, Kuroda *et al.* [24]	3998 ± 554	4209 ± 754	4873 ± 952
C15-3D, Mezzacappa *et al.* [13]	4110 ± 512	4675 ± 370	4975 ± 876
s15.nr, Andresen *et al.* [12]	3309 ± 555	3775 ± 875	4175 ± 576
M10-DD2, Morozova *et al.* [27]	1934 ± 634	2375 ± 772	2775 ± 902

corresponding Standard Deviation, (STD), for seven different Galactic sources at 1.0, 2.3, 3.1, 4.3, 5.4, 7.3, and 10 kpc. As we might expect, the number of triggers reduces with distance. As shown in Tables V and VI, the HFF slope estimation presents a higher STD. The results obtained using our methodology reflect that, this implementation could be applied to develop parameter estimation in upcoming LVK scientific runs. We leave this aspect for future publications.

ACKNOWLEDGMENTS

This work was supported by CONACyT Network Project No. 376127 *Sombras, lentes y ondas gravitatorias generadas por objetos compactos astrofísicos*. A. C. L. acknowledges a CONACYT scholarship. M. Z. was supported by NSF Grant No. PHY-1806885. A. M. was supported by the NSF Gravitational Physics Theory Program (No. PHY-1806692 and No. PHY-2110177).

[1] K. Kotake, K. Sato, and K. Takahashi, Explosion mechanism, neutrino burst and gravitational wave in core-collapse supernovae, Rep. Prog. Phys. **69**, 971 (2006).
[2] E. Abdikamalov, G. Pagliaroli, and D. Radice, Gravitational waves from core-collapse supernovae, in *Handbook of Gravitational Wave Astronomy*, edited by C. Bambi (Springer, Singapore, 2022), p. 21.
[3] J. Aasi *et al.* (LIGO Scientific Collaboration), Advanced LIGO, Classical Quantum Gravity **32**, 074001 (2015).
[4] F. Acernese, Advanced Virgo: A second-generation interferometric gravitational wave detector, Classical Quantum Gravity **32**, 024001 (2014).
[5] Y. Aso, Y. Michimura, K. Somiya, M. Ando, O. Miyakawa, T. Sekiguchi, D. Tatsumi, and H. Yamamoto, Interferometer design of the KAGRA gravitational wave detector, Phys. Rev. D **88**, 043007 (2013).
[6] H.-T. Janka, T. Melson, and A. Summa, Physics of core-collapse supernovae in three dimensions: A sneak preview, Annu. Rev. Nucl. Part. Sci. **66**, 341 (2016).
[7] B. Müller, The status of multi-dimensional core-collapse supernova models, Pub. Astron. Soc. Aust. **33**, e048 (2016).
[8] A. Mezzacappa, E. Endeve, O. E. B. Messer, and S. W. Bruenn, Physical, numerical, and computational challenges of modeling neutrino transport in core-collapse supernovae, Living Rev. Comput. Astrophys. **6**, 4 (2020).
[9] B. Müller, Hydrodynamics of core-collapse supernovae and their progenitors, Living Rev. Comput. Astrophys. **6**, 3 (2020).
[10] A. Burrows and D. Vartanyan, Core-collapse supernova explosion theory, Nature (London) **589**, 29 (2021).
[11] A. Mezzacappa, Toward realistic models of core collapse supernovae: A brief review, IAU Symp. **362**, 215 (2023).
[12] H. Andresen, B. Müller, E. Müller, and H.-T. Janka, Gravitational wave signals from 3d neutrino hydrodynamics simulations of core-collapse supernovae, Mon. Not. R. Astron. Soc. **468**, 2032 (2017).
[13] A. Mezzacappa, P. Marronetti, R. E. Landfield, E. J. Lentz, K. N. Yakunin, S. W. Bruenn, W. R. Hix, O. B. Messer, E. Endeve, J. M. Blondin, and J. A. Harris, Gravitational-wave signal of a core-collapse supernova explosion of a $15M_\odot$ star, Phys. Rev. D **102**, 023027 (2020).
[14] A. Mezzacappa, P. Marronetti, R. E. Landfield, E. J. Lentz, R. D. Murphy, W. Raphael Hix, J. A. Harris, S. W. Bruenn, J. M. Blondin, O. E. Bronson Messer, J. Casanova, and L. L. Kronzer, Core collapse supernova gravitational wave emission for progenitors of 9.6, 15, and $25M_\odot$, Phys. Rev. D **107**, 043008 (2023).
[15] H. Andresen, E. Müller, H. T. Janka, A. Summa, K. Gill, and M. Zanolin, Gravitational waves from 3D core-collapse supernova models: The impact of moderate progenitor rotation, Mon. Not. R. Astron. Soc. **486**, 2238 (2019).
[16] P. Cerdá-Durán, N. DeBrye, M. A. Aloy, J. A. Font, and M. Obergaulinger, Gravitational wave signatures in black hole forming core collapse, Astrophys. J. **779**, L18 (2013).
[17] K. Hayama, T. Kuroda, K. Kotake, and T. Takiwaki, Coherent network analysis of gravitational waves from three-dimensional core-collapse supernova models, Phys. Rev. D **92**, 122001 (2015).
[18] K. Hayama, T. Kuroda, K. Kotake, and T. Takiwaki, Circular polarization of gravitational waves from nonrotating

supernova cores: A new probe into the pre-explosion hydrodynamics, Mon. Not. R. Astron. Soc. **477**, L96 (2018).
[19] K. Hayama, T. Kuroda, K. Nakamura, and S. Yamada, Circular Polarizations of Gravitational Waves from Core-Collapse Supernovae: A Clear Indication of Rapid Rotation, Phys. Rev. Lett. **116**, 151102 (2016).
[20] H. Kawahara, T. Kuroda, T. Takiwaki, K. Hayama, and K. Kotake, A linear and quadratic time-frequency analysis of gravitational waves from core-collapse supernovae, Astrophys. J. **867**, 126 (2018).
[21] K. Kotake, W. Iwakami-Nakano, and N. Ohnishi, Effects of rotation on stochasticity of gravitational waves in the nonlinear phase of core-collapse supernovae, Astrophys. J. **736**, 124 (2011).
[22] K. Kotake, W. Iwakami, N. Ohnishi, and S. Yamada, Stochastic nature of gravitational waves from supernova explosions with standing accretion shock instability, Astrophys. J. Lett. **697**, L133 (2009).
[23] T. Kuroda, T. Fischer, T. Takiwaki, and K. Kotake, Core-collapse supernova simulations and the formation of neutron stars, hybrid stars, and black holes, Astrophys. J. **924**, 38 (2022).
[24] T. Kuroda, K. Kotake, K. Hayama, and T. Takiwaki, Correlated signatures of gravitational-wave and neutrino emission in three-dimensional general-relativistic core-collapse supernova simulations, Astrophys. J. **851**, 62 (2017).
[25] T. Kuroda, K. Kotake, and T. Takiwaki, A new gravitational-wave signature from standing accretion shock instability in supernovae, Astrophys. J. Lett. **829**, L14 (2016).
[26] T. Kuroda, K. Kotake, T. Takiwaki, and F.-K. Thielemann, A full general relativistic neutrino radiation-hydrodynamics simulation of a collapsing very massive star and the formation of a black hole, Mon. Not. R. Astron. Soc. **477**, L80 (2018).
[27] V. Morozova, D. Radice, A. Burrows, and D. Vartanyan, The gravitational wave signal from core-collapse supernovae, Astrophys. J. **861**, 10 (2018).
[28] B. Müller, H.-T. Janka, and A. Marek, A new multi-dimensional general relativistic neutrino hydrodynamics code of core-collapse supernovae. III. Gravitational wave signals from supernova explosion models, Astrophys. J. **766**, 43 (2013).
[29] J. W. Murphy, C. D. Ott, and A. Burrows, A model for gravitational wave emission from neutrino-driven core-collapse supernovae, Astrophys. J. **707**, 1173 (2009).
[30] K. Nakamura, T. Takiwaki, and K. Kotake, Three-dimensional simulation of a core-collapse supernova for a binary star progenitor of SN 1987a, Mon. Not. R. Astron. Soc. **514**, 3941 (2022).
[31] E. P. O'Connor and S. M. Couch, Exploring fundamentally three-dimensional phenomena in high-fidelity simulations of core-collapse supernovae, Astrophys. J. **865**, 81 (2018).
[32] C. D. Ott, E. Abdikamalov, P. Mösta, R. Haas, S. Drasco, E. P. O'Connor, C. Reisswig, C. A. Meakin, and E. Schnetter, General-relativistic simulations of three-dimensional core-collapse supernovae, Astrophys. J. **768**, 115 (2013).
[33] M. A. Pajkos, S. M. Couch, K.-C. Pan, and E. P. O'Connor, Features of accretion-phase gravitational-wave emission from two-dimensional rotating core-collapse supernovae, Astrophys. J. **878**, 13 (2019).
[34] M. A. Pajkos, M. L. Warren, S. M. Couch, E. P. O'Connor, and K.-C. Pan, Determining the structure of rotating massive stellar cores with gravitational waves, Astrophys. J. **914**, 80 (2021).
[35] K.-C. Pan, M. Liebendörfer, S. M. Couch, and F.-K. Thielemann, Equation of state dependent dynamics and multi-messenger signals from stellar-mass black hole formation, Astrophys. J. **857**, 13 (2018).
[36] K.-C. Pan, M. Liebendörfer, S. M. Couch, and F.-K. Thielemann, Stellar mass black hole formation and multi-messenger signals from three-dimensional rotating core-collapse supernova simulations, Astrophys. J. **914**, 140 (2021).
[37] J. Powell and B. Müller, Gravitational wave emission from 3d explosion models of core-collapse supernovae with low and normal explosion energies, Mon. Not. R. Astron. Soc. **487**, 1178 (2019).
[38] J. Powell and B. Müller, Three-dimensional core-collapse supernova simulations of massive and rotating progenitors, Mon. Not. R. Astron. Soc. **494**, 4665 (2020).
[39] J. Powell and B. Müller, Inferring astrophysical parameters of core-collapse supernovae from their gravitational-wave emission, Phys. Rev. D **105**, 063018 (2022).
[40] D. Radice, V. Morozova, A. Burrows, D. Vartanyan, and H. Nagakura, Characterizing the gravitational wave signal from core-collapse supernovae, Astrophys. J. **876**, L9 (2019).
[41] C. J. Richardson, M. Zanolin, H. Andresen, M. J. Szczepańczyk, K. Gill, and A. Wongwathanarat, Modeling core-collapse supernovae gravitational-wave memory in laser interferometric data, Phys. Rev. D **105**, 103008 (2022).
[42] S. Richers, C. D. Ott, E. Abdikamalov, E. O'Connor, and C. Sullivan, Equation of state effects on gravitational waves from rotating core collapse, Phys. Rev. D **95**, 063019 (2017).
[43] S. Scheidegger, R. Käppeli, S. C. Whitehouse, T. Fischer, and M. Liebendörfer, The influence of model parameters on the prediction of gravitational wave signals from stellar core collapse, Astron. Astrophys. **514**, A51 (2010).
[44] S. Shibagaki, T. Kuroda, K. Kotake, and T. Takiwaki, A new gravitational-wave signature of low-T/—W—instability in rapidly rotating stellar core collapse, Mon. Not. R. Astron. Soc. **493**, L138 (2020).
[45] S. Shibagaki, T. Kuroda, K. Kotake, and T. Takiwaki, Characteristic time variability of gravitational-wave and neutrino signals from three-dimensional simulations of non-rotating and rapidly rotating stellar core collapse, Mon. Not. R. Astron. Soc. **502**, 3066 (2021).
[46] V. Srivastava, S. Ballmer, D. A. Brown, C. Afle, A. Burrows, D. Radice, and D. Vartanyan, Detection prospects of core-collapse supernovae with supernova-optimized third-generation gravitational-wave detectors, Phys. Rev. D **100**, 043026 (2019).
[47] T. Takiwaki and K. Kotake, Anisotropic emission of neutrino and gravitational-wave signals from rapidly rotating core-collapse supernovae, Mon. Not. R. Astron. Soc. **475**, L91 (2018).
[48] D. Vartanyan and A. Burrows, Gravitational waves from neutrino emission asymmetries in core-collapse supernovae, Astrophys. J. **901**, 108 (2020).

[49] D. Vartanyan, A. Burrows, D. Radice, M. A. Skinner, and J. Dolence, A successful 3D core-collapse supernova explosion model, Mon. Not. R. Astron. Soc. **482**, 351 (2019).
[50] M. L. Warren, S. M. Couch, E. P. O'Connor, and V. Morozova, Constraining properties of the next nearby core-collapse supernova with multimessenger signals, Astrophys. J. **898**, 139 (2020).
[51] K. N. Yakunin, A. Mezzacappa, P. Marronetti, S. Yoshida, S. W. Bruenn, W. R. Hix, E. J. Lentz, O. E. Bronson Messer, J. A. Harris, E. Endeve, J. M. Blondin, and E. J. Lingerfelt, Gravitational wave signatures of *ab initio* two-dimensional core collapse supernova explosion models for 12–25$M_\odot$ stars, Phys. Rev. D **92**, 084040 (2015).
[52] P. Astone, P. Cerdá -Durán, I. D. Palma, M. Drago, F. Muciaccia, C. Palomba, and F. Ricci, New method to observe gravitational waves emitted by core collapse supernovae, Phys. Rev. D **98**, 122002 (2018).
[53] M.-A. Bizouard, P. Maturana-Russel, A. Torres-Forné, M. Obergaulinger, P. Cerdá-Durán, N. Christensen, J. A. Font, and R. Meyer, Inference of protoneutron star properties from gravitational-wave data in core-collapse supernovae, Phys. Rev. D **103**, 063006 (2021).
[54] A. Torres-Forné, P. Cerdá-Durán, M. Obergaulinger, B. Müller, and J. A. Font, Universal Relations for Gravitational-Wave Asteroseismology of Protoneutron Stars, Phys. Rev. Lett. **123**, 051102 (2019).
[55] B. Müller, H.-T. Janka, and A. Marek, A new multidimensional general relativistic neutrino hydrodynamics code for core-collapse supernovae. II. Relativistic explosion models of core-collapse supernovae, Astrophys. J. **756**, 84 (2012).
[56] S. M. Couch and C. D. Ott, Revival of the stalled core-collapse supernova shock triggered by precollapse asphericity in the progenitor star, Astrophys. J. **778**, L7 (2013).
[57] Z. Lin, C. Lunardini, M. Zanolin, K. Kotake, and C. Richardson, Detectability of standing accretion shock instabilities activity in supernova neutrino signals, Phys. Rev. D **101**, 123028 (2020).
[58] S. Mukherjee, L. Salazar, J. Mittelstaedt, and O. Valdez, New method for enhanced efficiency in detection of gravitational waves from supernovae using coherent network of detectors, Phys. Rev. D **96**, 104033 (2017).
[59] J. M. Antelis, M. Cavaglia, T. Hansen, M. D. Morales, C. Moreno, S. Mukherjee, M. J. Szczepań czyk, and M. Zanolin, Using supervised learning algorithms as a follow-up method in the search of gravitational waves from core-collapse supernovae, Phys. Rev. D **105**, 084054 (2022).
[60] M. D. Morales, J. M. Antelis, C. Moreno, and A. I. Nesterov, Deep learning for gravitational-wave data analysis: A resampling white-box approach, Sensors **21**, 3175 (2021).
[61] M. Cavaglià, S. Gaudio, T. Hansen, K. Staats, M. Szczepańczyk, and M. Zanolin, Improving the background of gravitational-wave searches for core collapse supernovae: a machine learning approach, Mach. Learn. Sci. Technol. **1**, 015005 (2020).
[62] M. J. Szczepań czyk, J. M. Antelis, M. Benjamin, M. Cavaglià, D. Gondek-Rosińska, T. Hansen, S. Klimenko, M. D. Morales, C. Moreno, S. Mukherjee, G. Nurbek, J. Powell, N. Singh, S. Sitmukhambetov, P. Szewczyk, O. Valdez, G. Vedovato, J. Westhouse, M. Zanolin, and Y. Zheng, Detecting and reconstructing gravitational waves from the next galactic core-collapse supernova in the advanced detector era, Phys. Rev. D **104**, 102002 (2021).
[63] Z. Lin, A. Rijal, C. Lunardini, M. D. Morales, and M. Zanolin, Characterizing a supernova's standing accretion shock instability with neutrinos and gravitational waves, Phys. Rev. D **107**, 083017 (2023).
[64] T. Bruel, M.-A. Bizouard, M. Obergaulinger, P. Maturana-Russel, A. Torres-Forné, P. Cerdá-Durán, N. Christensen, J. A. Font, and R. Meyer, Inference of protoneutron star properties in core-collapse supernovae from a gravitational-wave detector network, Phys. Rev. D **107**, 083029 (2023).
[65] S. Klimenko, S. Mohanty, M. Rakhmanov, and G. Mitselmakher, Constraint likelihood analysis for a network of gravitational wave detectors, Phys. Rev. D **72**, 122002 (2005).
[66] S. Klimenko, G. Vedovato, M. Drago, F. Salemi, V. Tiwari, G. Prodi, C. Lazzaro, K. Ackley, S. Tiwari, C. D. Silva, and G. Mitselmakher, Method for detection and reconstruction of gravitational wave transients with networks of advanced detectors, Phys. Rev. D **93**, 042004 (2016).
[67] S. Klimenko, I. Yakushin, A. Mercer, and G. Mitselmakher, A coherent method for detection of gravitational wave bursts, Classical Quantum Gravity **25**, 114029 (2008).
[68] M. Drago, S. Klimenko, C. Lazzaro, E. Milotti, G. Mitselmakher, V. Necula, B. O'Brian, G. A. Prodi, F. Salemi, M. Szczepanczyk, S. Tiwari, V. Tiwari, G. V, G. Vedovato, and I. Yakushin, coherent waveburst, a pipeline for unmodeled gravitational-wave data analysis, SoftwareX **14**, 100678 (2021).
[69] H. Andresen, E. Müller, H. T. Janka, A. Summa, K. Gill, and M. Zanolin, Gravitational waves from 3D core-collapse supernova models: The impact of moderate progenitor rotation, Mon. Not. R. Astron. Soc. **486**, 2238 (2019).
[70] J. Slutsky, L. Blackburn, D. A. Brown, L. Cadonati, J. Cain, M. Cavaglià, S. Chatterji, N. Christensen, M. Coughlin, S. Desai, G. González, T. Isogai, E. Katsavounidis, B. Rankins, T. Reed, K. Riles, P. Shawhan, J. R. Smith, N. Zotov, and J. Zweizig, Methods for reducing false alarms in searches for compact binary coalescences in LIGO data, Classical Quantum Gravity **27**, 165023 (2010).
[71] V. Necula, S. Klimenko, and G. Mitselmakher, Transient analysis with fast wilson-daubechies time-frequency transform, J. Phys. Conf. Ser. **363**, 012032 (2012).
[72] E. Cuoco *et al.*, Enhancing gravitational-wave science with machine learning, Mach. Learn. Sci. Technol. **2**, 011002 (2020).
[73] D. George and E. Huerta, Deep neural networks to enable real-time multimessenger astrophysics, Phys. Rev. D **97**, 044039 (2018).
[74] M. L. Chan, I. S. Heng, and C. Messenger, Detection and classification of supernova gravitational wave signals: A deep learning approach, Phys. Rev. D **102**, 043022 (2020).
[75] M. Ló pez, I. D. Palma, M. Drago, P. Cerdá-Durán, and F. Ricci, Deep learning for core-collapse supernova detection, Phys. Rev. D **103**, 063011 (2021).
[76] C. M. Bishop, *Pattern Recognition and Machine Learning (Information Science and Statistics)* (Springer-Verlag, New York, Inc., Secaucus, NJ, 2006).
[77] A. Burrows and D. Vartanyan, Core-collapse supernova explosion theory, Nature (London) **589**, 29 (2021).